Circulating non-coding RNAs in kidney disease

Zhao Q.

CHAPTER 4

Targeting long non-coding RNA *MALAT1* preserves endothelial cell integrity and protects against kidney fibrosis

Qiao Zhao[1], Loïs A.K. van der Pluijm[1], Atefeh Lafzi[2], Daniel Peled[3], Juliette A. de Klerk[1,4], Roderick C. Slieker[4], Leen M. 't Hart[4,5], Wendy Stam[1], Jacques M.G.J. Duijs[1], Angela Koudijs[1], Joris I. Rotmans[1], Hilal Kazan[6], Anton Jan van Zonneveld[1], Coen van Solingen[3] and Roel Bijkerk[1].

[1]Department of Internal Medicine (Nephrology) and the Einthoven Laboratory for Experimental Vascular Medicine, Leiden University Medical Center, Leiden, the Netherlands. [2] Graduate School of Informatics, Department of Health Informatics, Middle East Technical University, Ankara, Turkey. [3]Department of Medicine, Cardiovascular Research Center, New York University Grossman School of Medicine, New York, NY 10016, USA. [4]Department of Cell and Chemical Biology, Leiden University Medical Center, Leiden, The Netherlands. [5]Department of Biomedical Data Sciences, Section Molecular Epidemiology, Leiden University Medical Center, Leiden, The Netherlands. [6]Department of Computer Engineering, Antalya Bilim University, Antalya, Turkey.

Mol Ther Nucleic Acids. 2025;36(3):102689.

Abstract

Loss of integrity of the capillary network is directly associated with the development of kidney fibrosis resulting in chronic kidney disease. Here, we characterized long noncoding RNAs (lncRNAs) in endothelial cells (ECs) during the development of kidney fibrosis. Using a murine EC lineage-tracing model, we observed expression of the conserved lncRNA metastasis-associated lung adenocarcinoma transcript 1 (*Malat1)* to be elevated in ECs upon kidney injury; either by ischemia-reperfusion injury or unilateral ureteral obstruction (UUO). In addition, we found elevated *MALAT1* expression in the kidney and circulation of patients with fibrotic kidney diseases. Pharmacological intervention of *Malat1* initiated protection against fibrosis in the UUO model, illustrated by a marked decline in collagen deposition and a concomitant decrease in interstitial α-SMA positive cells in the kidney. This protective effect was further highlighted by an increase in capillary density and reduced endothelial to mesenchymal transition. Mechanistically, transcriptomic analyses of kidney ECs upon *Malat1* knockdown demonstrated increased EC-matrix-receptor interaction. Furthermore, we show that silencing of *MALAT1* results in increased barrier function and angiogenic response, less vascular leakage and decreased focal adhesions. Collectively, our findings classify the long non-coding RNA *MALAT1* as important regulator of EC function and kidney health. As such, targeting *MALAT1* may provide novel strategies to reduce kidney fibrosis.

Introduction

Chronic kidney disease (CKD) has a worldwide prevalence of >10%.[1] Besides its high morbidity, CKD is a leading cause of premature cardiovascular disease.[2] It is estimated that by 2040, CKD will become the 5th leading cause of death, due to the ageing population and increased prevalence of non-communicable diseases such as diabetes and hypertension.[3] Irrespective of the etiology, the common pathway in the pathology of CKD involves glomerular sclerosis, tubulointerstitial fibrosis associated with inflammation, myofibroblast proliferation, extracellular matrix accumulation and tubular atrophy.[4] A central feature of CKD is the progressive loss of the peritubular capillary network, a process that is referred to as rarefaction. Microvascular rarefaction is directly correlated with the severity of fibrosis[5] and the extent of rarefaction has been found to predict the degree of interstitial damage as well as changes in the glomerular filtration rate in CKD patients.[6] Likewise, emerging evidence indicates that the renal microvascular endothelium of the outer medullary peritubular network is the primary site of injury in kidney allograft nephropathy[7] and that regression of

the peritubular network is directly related to a decline in glomerular filtration, interstitial fibrosis and the severity of chronic allograft nephropathy.[8] These findings suggest an early, rate-limiting role for integrity of the peritubular capillary network in the pathogenesis of kidney fibrosis. Therefore, finding therapeutic strategies to stabilize the microvasculature in patients at risk for progressive renal failure may provide novel treatment options.

Emerging evidence suggests that long non-coding RNAs (lncRNAs) are critical regulators of gene regulatory networks in diverse biological processes, including kidney and endothelial cell (EC) (dys)function.[9,10] LncRNAs are defined as non-coding RNA transcripts longer than 200 nucleotides that exert structural and regulatory functions through their interaction with proteins, DNA or RNAs in the nucleus or cytoplasm.[11] LncRNAs have been demonstrated to be involved in gene regulation through a variety of mechanisms, such as epigenetic and transcriptional regulation through their association with chromatin-modifying complexes, regulation of mRNA processing and splicing; and acting as competitive inhibitors of endogenous RNAs (e.g., microRNAs).[11] An example of a lncRNA-directed function in kidney fibrosis can be found in lncRNA *lnc-TSI*, that was demonstrated to inhibit renal fibrogenesis by negatively regulating the TGF-β/Smad3 pathway.[12] Additionally, the lncRNAs RNA imprinted and accumulated in the nucleus (*Rian*) and myocardial infarction associated transcript (*Miat*) were shown to mediate myofibroblast formation in kidney fibrosis.[13] LncRNAs are also essential to EC function. For example, lncRNA activated by shear stress in endothelium (*LASSIE*) regulates shear stress sensing and endothelial barrier function through its association with and stabilization of junction proteins, e.g., Platelet endothelial cell adhesion molecule-1 (PECAM-1, CD31).[14]

In the current study we aimed to identify lncRNAs that are dysregulated in ECs during kidney fibrosis and to determine whether the modulation of lncRNA expression levels can augment the development of kidney fibrosis. To that end, we used a *Cdh5*-creER; tdTomato mouse model to genetically label ECs and isolated them through fluorescence-activated cell sorting from healthy kidneys and injured kidneys that were exposed to unilateral ureteral obstruction or ischemia reperfusion injury. Following lncRNA profiling of the sorted cells, we found a signature of differentially expressed lncRNAs in injured cells and demonstrate that lncRNA Metastasis Associated Lung Adenocarcinoma Transcript 1 (*MALAT1*) is part of a rate limiting post-transcriptional network involved in vascular integrity that can potentially be targeted to counteract kidney fibrosis.

Results

Kidney fibrosis is associated with loss of vascular integrity and endothelial-to-mesenchymal transition

To allow fate-tracing of ECs upon kidney injury we used a genetic mouse model expressing tamoxifen-inducible Cre driven by the *Cdh5* (VE-Cadherin) promoter (*Cdh5*-Cre-ERT2), as previously described,[15] and crossed these to Rosa-TdTomato$^{fl/fl}$ reporter mice, in which Cre-mediated excision resulted in Tomato expression specific to ECs. Next, we applied the unilateral ureter obstruction (UUO) model to induce severe kidney fibrosis. In addition, we included the unilateral ischemia-reperfusion injury (IRI) model as an acute kidney injury model, that associates with microvascular injury and develops kidney fibrosis in the longer term. At 10- and 2-days post-intervention, respectively, studies were terminated (**Fig. 1A**). In the UUO model, we observed that kidney fibrosis coincided with a loss of vascular integrity as illustrated by the altered appearance of fluorescent EC-derived tomato-signal (**Fig. 1B**). Notably, several tomato-positive cells appeared elongated and enlarged, suggesting that ECs possibly underwent endothelial-to-mesenchymal transition (EndMT). We co-stained the tomato-signal with mesenchymal marker alpha-smooth muscle actin (α-SMA) and indeed found several double-positive ECs, confirming that a fraction of ECs underwent EndMT (**Suppl. Fig. 1A**). We subsequently sorted the tomato-positive cells using fluorescence-activated cell sorting (FACS) (**Suppl. Fig. 1B**), and via qRT-PCR confirmed EndMT: acquirement of mesenchymal markers *α-SMA* (*Acta2*), and *Col-1α1* in ECs derived from UUO kidneys compared to ECs derived from healthy kidneys, while EC-markers *VE-cadherin (Cdh5)* and *Pecam-1/Cd31* were downregulated, suggesting loss of EC-phenotype (**Suppl. Fig. 1C-D**). Interestingly, in the IRI model, we observed a trend towards increased levels of mesenchymal marker *Col-1α1* in ECs already after 2 days, indicative of an early initiation of the profibrotic phenotype.

LncRNAs are differentially expressed in ECs during kidney injury

To implicate lncRNAs involved in the injury response of ECs in fibrotic kidney disease, we profiled lncRNAs in FACS-sorted *Cdh5*-derivative ECs isolated from injured and contralateral control kidneys. These efforts provided an EC-specific lncRNA signature within the *in vivo* kidney injury setting. Differential expression analysis and hierarchical clustering of lncRNA expression revealed clear differential lncRNA expression profile in ECs in diseased kidneys compared to healthy kidneys for both models (**Fig. 1C-D**). After IRI, we found 417 lncRNAs to

be significantly altered in ECs, of which 280 were decreased, and 137 increased. Upon UUO, 587 lncRNAs (322 down, 265 up) were dysregulated in ECs (-1 < logFC > 1, P < 0.05; **Fig. 1E**; **Suppl. Tables 1 and 2**). Simultaneously, mRNAs were profiled, and subsequent differential expression analysis, hierarchical clustering and pathway analyses revealed a clear differential mRNA expression profile in ECs in diseased kidneys compared to healthy kidneys (**Suppl. Fig. 2A-D; Suppl. Tables 3 and 4**). Gene Ontology (GO) biological process analysis of genes differentially expressed in ECs of both IRI and UUO models when compared to CLK indicates '*Actin Cytoskeleton Organization'* and '*Cell-Matrix Adhesion'* to be affected (**Suppl. Fig. 2E**).

Amongst differentially expressed lncRNAs, we found 17 lncRNAs that were differentially expressed in both models (**Fig. 1F**). Based on consistent upregulation in both injury models, as well as known conservation between mice and humans and previously reported increased circulating levels in patients with diabetic kidney disease,[16] we hypothesized that lncRNA *Malat1* may play an important role in ECs in kidney fibrosis and was selected to study further. Additionally, transcription factor motif enrichment analysis in the promoter regions of the differentially expressed lncRNAs identified among others HMGA1 to be enriched, and to potentially bind the promoter region of *MALAT1* (**Suppl. Fig. 3A-C**). Interestingly, HMGA1 has been linked to regulate EC function via controlling endothelial plasticity and angiogenesis[17-19]. We applied chromatin immunoprecipitation (ChIP) for HMGA1 and confirmed binding to the *Malat1* promoter by this transcription factor (**Suppl. Fig. 3D**), supporting direct regulation.

***MALAT1* is increased in human fibrotic kidney disease**

To demonstrate relevance for humans, we aimed to determine whether *MALAT1* dysregulation is consistent in human vascular and fibrotic kidney disease. We previously demonstrated that circulating *MALAT1* levels were increased in patients with diabetic kidney disease.[16] We reassessed circulating *MALAT1* levels in the plasma of these patients and confirmed increased *MALAT1* levels when compared to controls (**Fig. 2A**). Since circulating lncRNA levels are often carried in extracellular vesicles (EVs), we hypothesized that activated ECs may secrete increased levels of *MALAT1* in EVs. Indeed, when human umbilical vein endothelial cells (HUVECs) were stimulated with TGF-β and/or TNF-α, we observed increased *MALAT1* levels in EC-secreted EVs (**Fig. 2B**). Finally, we consulted online available datasets that contained transcriptomics data from human kidneys from patients with fibrotic kidney disease (GSE7392, GSE22459, GSE22459, GSE44131, GSE66494, GSE76882) and found an upregulation of *MALAT1* in the majority of datasets (**Fig. 2C**), which is consistent with our mouse studies. Importantly, in a single cell RNA-sequencing dataset that contained data from ECs in kidneys

from patients with diabetes with or without kidney fibrosis,[20] we observed that *MALAT1* is increased in ECs when kidney fibrosis is present (**Fig. 2C**).

***In vivo* knockdown of *Malat1* reduces kidney fibrosis and preserves vascular integrity**

Given the increase of *Malat1* in ECs in UUO and IRI, we hypothesized that knockdown of *Malat1* may protect against disturbed microvascular integrity and the subsequent development of kidney fibrosis. To investigate this, we applied the UUO model in the *Cdh5*-creER;tdTomato mice while inhibiting *Malat1* expression using intraperitoneal injection of *Malat1*-targeting GapmeRs. Silencing of *Malat1* in the kidneys was confirmed by qRT-PCR (**Fig. 3A**), as well as by *in situ* hybridization (ISH) for *Malat1* within the kidney tissue (**Fig. 3B-C**). Interestingly, ISH indicates that upon UUO, *Malat1* is elevated in the kidney cortex, while gap*Malat1*-mediated knockdown also occurs mainly in the kidney cortex. To assess whether *Malat1* knockdown resulted in decreased kidney fibrosis, we next used a Sirius Red staining to determine collagen deposition (**Fig. 3D**). Indeed, we observed a strong decrease in kidney fibrosis upon inhibition of *Malat1*, amounting to a ~50% reduction in collagen deposition (**Fig. 3E**). Furthermore, we observed a marked reduction in the number of α-SMA positive myofibroblasts in kidneys from the gap*Malat1* mice, compared to kidneys of gapC-treated mice, 10 days after UUO (**Fig. 3F-G**). We confirmed this decrease in kidney α-SMA expression upon *Malat1* inhibition using Western blot (**Fig. 3H-I**). Given the observed role of *Malat1* in regulating EC function, we then determined the impact of *Malat1* knockdown on renal vascular integrity after UUO. Indeed, we observed that the density of MECA32+ peritubular capillaries in the gap*Malat1*-treated mice was markedly higher than in the control kidneys (**Fig. 3J-K**). Similarly, we observed higher levels of tdTomato+ VE-cadherin(-derived) cells upon *Malat1* knockdown (**Fig. 3L-M**). Given that our lineage trace model allows fate tracing of the ECs, we next assessed whether also EndMT was affected by silencing *Malat1*. Indeed, we found decreased numbers of α-SMA-tdTomato double positive cells, indicating a decrease in EndMT (**Suppl. Fig. 4**). Taken together, these data further confirm that *Malat1* plays an important function *in vivo* in regulating vascular integrity and thereby in mediating kidney fibrosis.

Knockdown of *MALAT1* affects cell-cell and cell-matrix interaction in ECs

To understand how depletion of *MALAT1* preserves vascular integrity and decreases fibrosis and myofibroblast formation, we isolated RNA from FACS-sorted VE-cadherin;tdTomato+ cells in the UUO model (10 days) after silencing *Malat1* and performed transcriptomic analysis by

RNA-sequencing (RNA-seq). Unsupervised hierarchical clustering of genes differentially expressed in *Malat1*-sufficient and -deficient ECs revealed that *Malat1* significantly reprogrammed transcriptional responses in response to UUO induction (**Fig. 4a, -**1 < logFC > 1, P<0.05**; Suppl. Table 5**). In addition, using qRT-PCR we confirmed knockdown of *Malat1* in the sorted VE-cadherin-tdTomato+ cells (**Fig. 4B**). Gene set enrichment analysis of differentially expressed genes identified that '*ECM-Receptor Interaction*' is activated, while metabolic and mitochondrial pathways are suppressed (**Fig. 4C**). In addition, analysis of enriched cellular components indicates *'Focal Adhesion'* and *'Cell-Substrate Junction'* are affected (**Fig. 4D**). These pathway analyses were confirmed by Ingenuity pathway analysis (IPA) that also indicated increased '*Focal Adhesion Kinase (FAK) signaling'*, important for cell-matrix interactions, and impaired metabolic pathways, mainly reduced '*Oxidative Phosphorylation'* and increased '*Mitochondrial Dysfunction'* (**Suppl. Fig. 5**). As such, these data pose two possible mechanisms (cell-matrix/cell-cell interactions and metabolic/mitochondrial function) via which *Malat1* affects EC function and kidney fibrosis.

To further explore this, we started out with testing the effect of *MALAT1* knockdown in HUVECs on mitochondrial function *in vitro* using Seahorse respirometry. Under basal conditions, *MALAT1* knockdown increased oxygen consumption in ECs (**Suppl. Fig. 6A**), corresponding to increased basal respiration, maximal respiration and proton leak (**Suppl. Fig. 6B**). Upon TGF-β treatment, simulating the *in vivo* activated state, gap*MALAT1* treated HUVECs displayed decreased oxygen consumption corresponding to a trend towards decreased basal respiration, maximal respiration and proton leak (**Suppl. Fig. 6A-B**). While the latter is in line with the RNA-seq data showing decreased mitochondrial function and oxidative phosphorylation, this presumably negative effect may not solely explain the beneficial effects of *Malat1* knockdown *in vivo*. Therefore, we further investigated the role of *MALAT1* in cell-cell and cell-matrix interactions and FAK signaling, as identified under **Fig. 4C-D**. When visualizing relative gene expression from genes involved in the ECM-receptor interaction pathway, it is apparent that decreased *Malat1* levels result in higher levels of many of these genes (**Fig. 4E**). Following this notion, we next examined cell-cell and cell matrix interaction by staining HUVECs for VE-cadherin and F-actin to visualize the actin fibers. While we did not find differences in absolute VE-cadherin staining, a clear decrease in cell-cell contacts was visible upon measuring the number of gaps between cells and gap area (**Fig. 4F-J**). More importantly, when analyzing focal adhesion junctions (FAJs), a measure of EC activation and junction remodeling[21], we found a reduction these FAJs upon *MALAT1* knockdown (**Fig. 4K**), indeed implicating a more stable cell-matrix interaction, which is in line with **Fig. 3** demonstrating that *MALAT1* knockdown preserves vascular integrity.

MALAT1* potentially acts *in trans* and *in cis

We next sought to gain more insight into the possible underlying molecular mechanisms of *MALAT1* in EC function. First, we performed FISH for *MALAT1* on HUVECs and confirmed nuclear localization (**Suppl. Fig. 7**). As it was previously indicated that *MALAT1* plays a *cis*-regulatory role in gene transcription,[22] we performed virtual chromosome conformation capture followed by high-throughput sequencing (Hi-C) analysis to identify coregulatory genes and potential *in cis* mechanisms driven by *MALAT1* in its genomic locus.[23] *MALAT1* appears to have a strong association with nearby genes, potentially *FAUP4* and *NEAT1* (**Suppl. Fig. 8A-B**). Increased *Neat1* expression upon *Malat1* knockdown was confirmed in our RNA-seq dataset (**Suppl. Fig. 8C**). These data suggest a relation between *Malat1* and the genes in its topological associated domain, indicating a potential *cis*-regulatory effect of *Malat1* depletion in kidney ECs. Next, we investigated the potential *in trans* functional roles of *MALAT1.* We identified '*RNA Binding*' to be the top enriched molecular function in our RNA-seq dataset (**Suppl. Fig. 8D**), and found a strong overlap with genes involved in RNA-binding by chromatin-associated proteins (**Suppl. Fig. 8E**).[24,25] These data prompted us to analyze the presence of potential RNA-binding domains in *MALAT1* and found a strong enrichment of the PF00076 RNA recognition motif **(Suppl. Fig. 8F)**. Using CatRAPID, we subsequently found numerous RNA-binding proteins that are predicted to directly interact with *MALAT1* and *Malat1* (**Suppl. Fig. 8G**). Most strikingly, we found polycomb protein SUZ12 to be the top hit, while ChIP-X Enrichment Analysis on the differentially expressed genes from our RNA-seq indeed identified SUZ12 and enhancer of zeste homolog 2 (EZH2), that together with SUZ12 forms the polycomb repressive complex 2 (PRC2), to be the strongest associated transcription factors (**Suppl. Fig. 8H**). Following this notion, this interaction of *MALAT1* has been previously confirmed,[26,27] and suggests the nuclear *MALAT1* may be involved in ECs in *in trans* chromatin binding and transcriptional regulation via SUZ12 and the PRC2.

***In vitro* knockdown of *MALAT1* inhibits endothelial cell activation**

Given our findings that *MALAT1* inhibition preserves vascular integrity and affects cell-cell/cell-matrix contacts we next set out to determine whether *MALAT1* knockdown indeed impacts EC and vascular function. First, as we observed EndMT to occur during kidney fibrosis, we used our *in vitro* mouse EC model for EndMT[28] to investigate the role of *MALAT1*, and showed that TGF-β induces *Malat1* expression (**Suppl. Fig. 9A**). However, *Malat1* knockdown did not prevent the TGF-β induced elongation of the cells associated with EndMT (**Suppl. Fig. 9B-C**), nor the increase in mesenchymal marker α-SMA (**Suppl. Fig. 9D-E**). *Malat1* silencing

decreased secreted pro-collagen1α1 levels (**Suppl. Fig. 9F**), while *α-SMA* and *col1α1* gene expression were not affected (**Suppl. Fig. 9G**). These data suggest that reducing cellular *Malat1* levels may not affect the cellular transition but could influence pro-fibrotic properties. Next, we knocked down *MALAT1* in HUVECs using GapmeR antisense oligonucleotides (gap*MALAT1*) or control GapmeRs (gapC) and performed a series of functionality assays. First, we assessed the angiogenic response of HUVECs treated with gap*MALAT1* in the Organoplate® microfluidic system-based angiogenesis assay and found that silencing of *MALAT1* resulted in less angiogenesis (**Fig. 5A**) as shown by reduced sprout length and area (**Fig. 5B-C**). Then, the endothelial barrier function was assessed by trans-endothelial electrical resistance measurements of HUVECs. Silencing of *MALAT1* expression increased the capacity of HUVECs to form a tight barrier (**Fig. 5D**). In line with the data provided in **Fig. 4**, application of mathematical modeling (provided by the ECIS software) indicated that the increased barrier function upon knockdown of *MALAT1* was driven by significantly enhanced cell-cell contacts as well as a trend towards more efficient cell-matrix contacts (**Fig. 5E**). Since a tight barrier prevents vascular leakage, we leveraged the Organoplate® microfluidic system,[29] to test the effect of *MALAT1* depletion on the ability of HUVECs to form a leak tight 3D capillary-like vessel. Perfusion of these capillary-like vessels with fluorescently labeled albumin allows measurement of its potential leakage through the vessel (**Fig. 5F**). We observed that *MALAT1* knockdown in HUVECs leads to decreased vascular leakage when compared to gapCTRL (**Fig. 5G-H**). Collectively, *MALAT1* emerges to be an important regulator in driving EC integrity/barrier function and activation.

Discussion

In this study we demonstrate that lncRNA *MALAT1* is strongly increased in ECs during the fibrotic response upon kidney injury. Knockdown of *Malat1* inhibited EC activation and resulted in preserved vascular integrity in the kidney and decreased kidney fibrosis Together, our findings support a faciliatory role for *MALAT1* negatively impacting vascular integrity in reverberating kidney fibrosis.

Cell-matrix and cell-cell interactions are vital to ECs to maintain stable barrier function and integrity of the blood vessels.[30] We found that knockdown of *MALAT1,* using antisense oligonucleotides *in vitro,* increased barrier function, decreased vascular leakage, preserved cell-cell contacts and decreased the formation of focal adhesion junctions, all features of activation and remodeling of ECs.[21] In addition, we observed decreased angiogenesis, which corroborates with previous reports showing that depletion of *MALAT1* inhibits the angiogenic

response of ECs,[31,32] as well as other studies demonstrating a pathogenic role of *MALAT1* in EC dysfunction.[33,34] Given the increase in *MALAT1* levels upon kidney injury both in humans and mice, these data clearly point towards a role for *MALAT1* in activation of ECs and loss of vascular integrity, that may be averted by using GapmeRs *in vivo* to inhibit *MALAT1*. Indeed, we show in the UUO model that this approach results in silencing of *MALAT1* followed by preserved kidney vascular integrity and suppression of kidney fibrosis.

To gain more insight into *MALAT1*'s *in cis* and *in trans* molecular mechanisms we performed *in silico* analyses on our *in vivo* transcriptomics data and identified a potential regulatory role for *MALAT1* via SUZ12, a member of the repressive complex PRC2, which is important in chromatin regulation and transcriptional repression.[35] Supporting this notion, it has indeed been previously demonstrated that *MALAT1* can both directly bind SUZ12,[26] and is important in transcriptional regulation via chromatin interactions.[27,36,37] Moreover, PRC2 has been found to decrease integrin expression in ECs and is important in maintenance of vascular health, [45,46] while a strong link has been found between VE-cadherin expression and PRC2/SUZ12-mediated regulation of an EC-transcriptional program involved in vascular stability.[38] As such, a picture emerges that *MALAT1* is involved in chromatin regulation and transcription via binding SUZ12 leading to repression of a transcriptional program involved in maintaining EC function, possibly in conjunction with its neighboring lncRNA *NEAT1*,[27,39] that our data suggest are co-regulated.

While many studies also describe a role for *MALAT1* as competing endogenous RNA for microRNA, including in the setting of kidney fibrosis,[40] our data suggest *MALAT1* functions as a transcriptional regulator. The subcellular localization of *MALAT1*, that we, and others,[27,41] confirmed to be prominent in the nucleus, suggests that *MALAT1* functions in the nucleus and has a less significant role in sponging (cytoplasmic) microRNAs.

While we find a clear effect of *MALAT1* knockdown on EC function, it cannot be excluded that the protective effect that is observed by *MALAT1* silencing *in vivo*, is also mediated through other cell types. For example, *MALAT1* regulates differential activation of macrophages,[42] and mediates podocyte injury,[43] that may contribute to the development of kidney fibrosis. In addition, *MALAT1* is also highly expressed in tubular epithelial cells, where we, upon GapmeR treatment, also observe knockdown using ISH. However, as it was previously found that *MALAT1* silencing in HK-2 kidney epithelial cells did not result in any functional alteration, but mainly altered EC function, this suggests at least a partial regulatory function for *MALAT1* in ECs.[44]

Next to increased levels of *MALAT1* in mouse kidneys, we observed upregulation of (endothelial) *MALAT1* in human fibrotic kidney disease. Furthermore, we validated that circulating levels of *MALAT1* are increased in human fibrotic kidney disease, which is in line with previous reports.[16,44,45]. Interestingly, since most circulating lncRNAs are carried by EVs, it is tempting to speculate that ECs may be responsible for increased secretion of EVs containing *MALAT1*. Especially as it has been demonstrated that upon kidney injury, more activated EC-derived EVs appear in the circulation.[46,47] Moreover, high glucose levels increase total HUVEC-derived EVs.[48] Following this, our *in vitro* studies indicate that activated ECs secrete more EV-carried *MALAT1*, suggesting this may indeed be the reason for the higher circulating *MALAT1* levels as observed in patients with kidney disease.

Taken together, our studies identify *MALAT1* as an important regulator of EC function potentially driving kidney fibrosis. Silencing *MALAT1* reduced fibrosis by preserving vascular integrity and therapies aimed at inhibiting *MALAT1* in the vasculature may serve as potential treatment for chronic kidney disease.

Materials and Methods

Animals

All animal experiments were approved by the animal welfare committee of the veterinary authorities of the Leiden University Medical Center. Standard chow diet and drinking water were provided ad libitum. Eight week old male B6.Cdh5-Cre-ERT2;tdTomato mice were used, in which tamoxifen inducible Cre-mediated excision results in endothelial Tomato expression. Mice received intra-peritoneal 2mg/0.2mL tamoxifen for 5 consecutive days. The UUO model was performed through a left flank incision, followed by identification of the ureter and double ligation thereof close to the lower pole of the kidney with two separate silk ties. After 10 days the mice were killed. For the *Malat1* GapmeR experiment, LNA control GapmeR or LNA *Malat1* GapmeR (20 mg/kg; Exiqon) were injected intraperitoneally twice: 2 days before and 2 days after UUO surgery. The unilateral IRI model was performed via an abdominal incision, after which the renal artery and vein were identified and, using surgical clamps (S&T, Neuhausen, Switzerland), unilaterally clamped for 45 min. The contralateral kidneys were used as controls. After 2 days the mice were killed. Kidneys were removed and RNA and protein were isolated as described elsewhere.

LncRNA and mRNA profiling

Profiling of lncRNAs and mRNAs was performed by Arraystar Inc according to protocol using the Agilent Array platform. Sample preparation and microarray hybridization were based on standard protocols of the manufacturer with minor modifications. In brief, mRNA was purified from total RNA after rRNA removal (mRNA ONLY^{TM} Eukaryotic mRNA Isolation Kit, Epicentre). Each sample was then amplified and transcribed into fluorescent cRNA along the full length of transcripts without bias using a mix of oligo(dT) and random primers (Arraystar Flash RNA Labeling Kit, Arraystar). Labeled cRNAs were then hybridized on the "Mouse lncRNA Array v3.0" (8K x 60K, containing 35923 lncRNAs and 24881 coding transcripts, Arraystar). After washing the slides, the arrays were scanned on Agilent Scanner G2505C. Agilent Feature Extraction software (version 11.0.1.1) was used for analysis of acquired array images. GeneSpring GX v12.1 software package (Agilent Technologies) was used to perform quantile normalization and data processing. Following quantile normalization of raw data, lncRNAs and mRNA with at least 6 out of 12 samples having flags in Present or Marginal ("All Targets Value") were selected for further data analysis. Statistically significant differentially expressed lncRNAs and mRNAs between the two groups were identified through Volcano Plot filtering.

Cell culture

Primary human umbilical vein endothelial cells (HUVECs) were isolated from human umbilical cords as previously described59 and cultured on 1% gelatin coated surfaces in endothelial cell growth medium 2 (EGM2; C-39216, PromoCell, Germany) supplemented with antibiotics. Where indicated, HUVECs were treated with 10 ng/mL TGF-β1 and/or 10 ng/mL TNF-α (Sigma). Mouse embryonic endothelial cells (MEECs), as previously described,[29] were cultured on 1% (w/v) gelatin coating in Dulbecco's modified Eagle medium (Gibco/Invitrogen, Breda, the Netherlands) supplemented with 10% fetal calf serum and 2 mM L-glutamine (Invitrogen). MEECs were treated for 48 hours with 2 ng/mL TGF-β3 (Peprotech, London, UK). Cells were transfected at 60% to 75% confluence with 50-100 nM locked nucleic acid (LNA) GapmeR (Exiqon, Vedbaek, Denmark) targeting MALAT1/Malat1 or control gapmer using Lipofectamine 3000 (Life Technologies, Carlsbad, CA) according to the manufacturer's protocol.

FACS sorting

Kidneys were extracted from three individual mice per injury model and mechanically dissociated and filtered through 100 and 40 μm filters. The obtained cell suspension was then sorted on the FACSAria II (BD Biosciences, Franklin Lakes, NJ, United States).

Cell debris was gated out using a FSC-A/SSC-A plot (gate 1), doublets were gated out using a SSC-W/ SSC-H plot (gate 2) and a FSC-W/FSC-H plot (gate 3), and these three gates were combined. Next, from the combined exclusion gate, cells that were positively identified having a fluorescent tomato signal were collected.

RNA isolation and qRT-PCR analysis

Total RNA was isolated using Trizol reagent (Invitrogen) combined with the RNeasy Micro Kit (Qiagen, The Netherlands) and reverse transcribed using Iscript (Bio-Rad) according to the manufacturers protocol. Quantitative PCR (qRT-PCR) of target genes was performed using SYBR Green Master Mix (Applied Biosystems). Used primer sequences of target genes were: α-SMA (sense) CGTGGCTATTCCTTCGTGAC; α-SMA (antisense): GCGTTCGTAGCTCTTCTCC; Col1 α1 (sense): TGACTGGAAGAGCGGAGAGT; Col1α1 (antisense): GTTCGGGCTGATGTACCAGT; β-actin (sense): AGGTCATCACTATTGGCAACGA; β-actin (antisense): CCAAGAAGGAAGGCTGGAAAA. For *MALAT1/Malat1*, mouse and human Taqman assays were used (Thermo Fisher Scientific, Waltham, MA). Gene expression levels were normalized to β-actin and quantified using the delta delta Ct method.

GapmeRs

The locked nucleic acid (LNA) GapmeRs for *MALAT1* (human MALAT1: transcript variant ENST00000619449, mouse Malat1: transcript variant ESMUST00000173314) were obtained from Exiqon (Vedbaek, Denmark). Negative control A GapmeR was used as negative control.

Western Blot

Western blot was performed on lysates harvested in lysis buffer (50 mM Tris-HCl pH7.5, 150 mM NaCl, 1% SDS, 0,5% deoxycholate, 0,5% Triton X-100) with the addition of protease inhibitors (Complete protease inhibitor cocktail, Roche, Basel, Switzerland). BCA Protein Assay Kit (Pierce) was used to determine total protein content and 5–20 µg. of total protein was applied on Any-kD Mini-PROTEAN TGX Precast SDS page gels (Biorad). Gels were transferred to nitrocellulose membranes using the Trans-Blot Turbo Transfer System (Biorad) and blocked with 5% non-fat milk powder in PBS with 0.01% of Tween (PBST). Primary antibodies against the following proteins were used: α-SMA (R&D, Minneapolis, MN, USA), GAPDH (Cell Signaling Technology, Leiden, The Netherlands). Membranes were incubated with these primary antibodies overnight at 4 °C, followed by incubation with appropriate secondary HRP-labeled antibodies for 1 hr. at room temperature. Upon PBST washing, membranes were incubated with SuperSignal West Dura Chemiluminescent Substrate

(Thermo Fisher Scientific)). Quantification of the protein bands was performed using ImageJ software and normalized to GAPDH.

Immunohistochemistry

Kidneys were fixed in 4% PFA for 1 h at 4°C, cryopreserved in 20% sucrose, and frozen in liquid nitrogen. Five micrometers sections were stained for α-SMA and MECA32 using a mouse fluorescein isothiocyanate-conjugated antibody against α-SMA (Sigma), or a specific antibody against MECA32 (Becton Dickinson, Franklin Lakes, New Jersey, USA) followed by the corresponding Alexa-secondary antibodies (Invitrogen). For Picro Sirus Red (PSR), kidneys were sagittally sectioned and fixed in 10% neutral buffered formalin, processed and embedded in paraffin wax. After sectioning, section was dehydration, xylene clearing and mounting, sections were imaged using 3D Histech Pannoramic MIDI Scanner (Sysmex). PSR staining for collagen deposition was performed by a 1-hour incubation of the sections in 0.1% Sirius Red solution, followed by 2 rinses in 1% acidic acid. Staining was quantified over the entire kidney section using HistoQuant software (3D HISTECH, Hungary) or ImageJ software (NIH, Bethesda, MD, USA). Staining of HUVECs for VE-cadherin and F-actin was performed by seeding HUVECs on an 8-well Ibidi plate and fixation with 4% paraformaldehyde (Added Pharma 1642810) and permeabilization with Triton-X100 (Merck 11869). 5% BSA was used to block non-specific antigens. HUVECs were incubated with mouse anti-human CD144 (VE-cad) primary antibody (BD Pharmingen 555661) and then secondary IgG goat anti mouse Alexa 488 (Invitrogen A32723), 1:200 Phalloidin-TRITC (Sigma P1951), 1:2000 Hoechst (Thermo Fisher H3569). Images were taken using a high content confocal microscope (Molecular Devices, ImageXpress™ Micro Confocal), For determining FAJ junctions: the cell boundary was identified by VE-cad staining and the length of the boundary was measured using the length measurement tool in ImageJ. The cell-cell junction pattern is determined by the relative orientation of f-actin and membrane. The f-actin on FAJ was perpendicular to the cell membrane, while the f-actin bundle is parallel to the cell membrane on mature junctions.30 The FAJ length of the selected cell was measured, and the ratio of the FAJ length to the total length was calculated to obtain the FAJ ratio of each cell.

Vascular leakage and angiogenesis assay

HUVECs were used to culture 3D capillary-like vessels on the Organoplate® microfluidic system (Mimetas, 9603-400B) and used to assess leakage/permeability based on the method described by van Duinen et al.[29] After 7 days, the capillary-like vessels were used to assess

permeability by adding Alexa 555-labeled albumin (75 µg/mL, Invitrogen, A34786) to the perfusion channel followed by assessment of leakage of albumin to the gel channel over a time period of 30 min using the ImageXpress confocal microscope (Molecular Devices). Quantification of vascular leakage was performed using ImageJ as previously described.[29] For the angiogenesis assay the same platform with the 3D capillary-like vessels on the Organoplate® microfluidic system was used and performed as described previously.[50] In short, angiogenic sprouts were stimulated with VEGF + bFGF + S1P for 4 days, where the last 48 hours were in the presence of MALAT1 and control GapmeRs. Angiogenic factors were used in the following concentrations: 50 ng/mL for VEGF, 50 ng/mL for bFGF, and 500 nM for S1P. Sprouting was visualized with phalloidin staining (Sigma-Aldrich) and imaged using a high content confocal microscope (Molecular Devices, ImageXpress™ Micro Confocal). Total sprouting area and average sprouting length were quantified using ImageJ by manually determining the distance between the microvessel and the (tip) cell sprouting furthest into the gel.

Endothelial barrier function

Using the electric cell-substrate impedance sensing system (ECIS Zθ, Applied Biophysics) and ECIS plates (96W20idf PET, Applied Biophysics), endothelial barrier function was assessed by measuring trans-endothelial electrical resistance (TEER), as previously described.[49] Multiple frequency/time (MFT) mode was used to assess the barrier and results are expressed as relative resistance at a frequency of 4,000 Hz. Using impedance data, ECIS software was used for further mathematical modeling to calculate the cell morphological parameters of cell-cell (Rb) and cell-matrix (α) contacts.

ELISA

The mouse Pro-Collagen I alpha 1 ELISA (Abcam) was performed on cell lysates according to the instructions of the manufacturer.

Mitochondrial respiration

Oxygen consumption rate (OCR) and corresponding analyses of basal respiration, maximal respiration and proton leak were measured using the Seahorse XF96 analyzer and its associated Wave software (Agilent Technologies).

In Situ Hybridization

Chromogenic in situ detection was performed on formalin-fixed paraffin-embedded (FFPE) mouse kidney tissue sections using the RNAscope in situ hybridization (ISH) technology (Advanced Cell Diagnostics, Bio-Techne, Minneapolis, MN). 5-µm sections were used and deparaffinized followed by boiling with RNAscope Target Retrieval Reagent for 15 minutes at 99°C and subsequent protease digestion for 30 min at 40°C. Hybridization was performed at 40°C for 2 hr with RNAscope Probe - Mm-Malat1 (313391, Advanced Cell Diagnostics). RNAscope® Negative Control Probe_dapB (310043) and RNAscope Probe - Mm-Ppib (313911) were used as negative and positive controls, respectively. RNAscope 2.5 HD Reagent Kit (Brown) (322310) was used to visualize the bound probes.

RNA-sequencing and pathway analysis

RNA-sequencing on FACS-sorted tdTomato positive cells from mouse kidneys after the mice were treated with MALAT1 or control GapmeR was performed by Novogene (Cambridge, UK). In short, sequencing libraries were generated using NEBNext® UltraTM RNA Library Prep Kit for Illumina® (NEB, USA) following manufacturer's recommendations. mRNA was purified from total RNA using poly-T oligo-attached magnetic beads. Fragmentation was carried out using divalent cations under elevated temperature in NEBNext First Strand Synthesis Reaction Buffer (5X). First strand cDNA was synthesized using random hexamer primer and M-MuLV Reverse Transcriptase (RNase H-). Second strand cDNA synthesis was subsequently performed using DNA Polymerase I and RNase H. Remaining overhangs were converted into blunt ends via exonuclease/polymerase activities. After adenylation of 3' ends of DNA fragments, NEBNext Adaptor with hairpin loop structure were ligated to prepare for hybridization. In order to select cDNA fragments of preferentially 150~200 bp in length, the library fragments were purified with AMPure XP system (Beckman Coulter, Beverly, USA). Then 3 µl USER Enzyme (NEB, USA) was used with size-selected, adaptor ligated cDNA at 37 °C for 15 min followed by 5 min at 95 °C before PCR. Then PCR was performed with Phusion High-Fidelity DNA polymerase, Universal PCR primers and Index (X) Primer. At last, PCR products were purified (AMPure XP system) and library quality was assessed on the Agilent Bioanalyzer 2100 system. Sequencing reads were aligned to the mouse genome (GRCm39 M33) using STAR (v2.7.7a). Mapped reads were quantified for genomic features with featureCounts. For differential expression analysis, a quasi-likelihood negative binomial generalized log-linear model was applied using the edgeR package (v3.18) in R. Read counts were normalized using the Trimmed Mean of M-values (TMM) method. Genes were considered differentially expressed if the contrast between conditions reached statistical significance, defined by a false discovery rate (FDR)-adjusted p-value of less than 0.05. All statistical analyses were performed in R (v4.4.0). Normalized data were used for

gene-set and GO enrichment analysis. Additional (pathway) analyses, where indicated, were performed using Enrichr, Ingenuity Pathway Analysis (IPA) software and Rummagene. Morpheus tool (Broad institute, https://software.broadinstitute.org/morpheus/) was used to visualize gene expression in a max projection heatmap.62

Transcription factor motif enrichment, CatRAPID and HiC

Discovery of enriched transcription factor binding site motifs within lncRNA promoter regions (defined as 2000 bp upstream of transcription start site) was performed by the analysis of Motif Enrichment (AME) tool, using the JASPAR general database. The catRAPID algorithm (PMID: 34086933) was used to determine RNA-binding domains, RNA binding proteins in Malat1 and MALAT1. We visualized the 3-dimensional (3D)-architecture within the genetic locus of MALAT1 and Malat1 using high-throughput chromosome conformation capture (Hi-C) (PMID: 19815776) data from the 3D genome browser (PMID: 30286773) in HUVECs (PMID: 25497547) and C2C12 (PMID: 29654311)

Chromatin Immunoprecipitation

Mouse embryonic endothelial cells (MEECs) were used to perform chromatin Immunoprecipitation (ChIP) on HMGA1 with 10 µg anti-HMGA1a / HMGA1b antibody - ChIP Grade (ab4078, Abcam) or negative control IgG using the EZ-Magna ChIP™ A/G Chromatin Immunoprecipitation Kit (Merck-Millipore) according to the instructions of the manufacturer. Data were normalized with inputs. PCR primers that were used to detect Malat1 promoter region on the immunoprecipitated DNA were as follows: mmu-Malat1-promoter-bus/ree-fw AGCTTTAATCCAGCACTTGTGTAAG; mmu-Malat1-promoter-bus/ree-rev GGAGGTCCAGTGTTAGACCATT; mmu-Malat1-promoter-jaspar-fw GACGGGTTCCGCGGTC; mmu-Malat1-promoter-jaspar-rev CCAGGTCTATCTCATCGCTTCC; mmu-Malat1-promoter-manabe-fw GAAACATCTGAAAAACTTGGGGCT; mmu-Malat1-promoter-manabe-rev GGCCTCTTGGACCTTGCTAATA.

Statistical analyses

Results are expressed as mean ± standard error of the mean (SEM), unless otherwise indicated. Statistical analyses were performed using student's T-test or one-way ANOVA. $P<0.05$ was considered statistically significant. For IPA, bias corrected z-scores were determined with a z-score higher than 2 or lower than -2 being considered statistically significant.

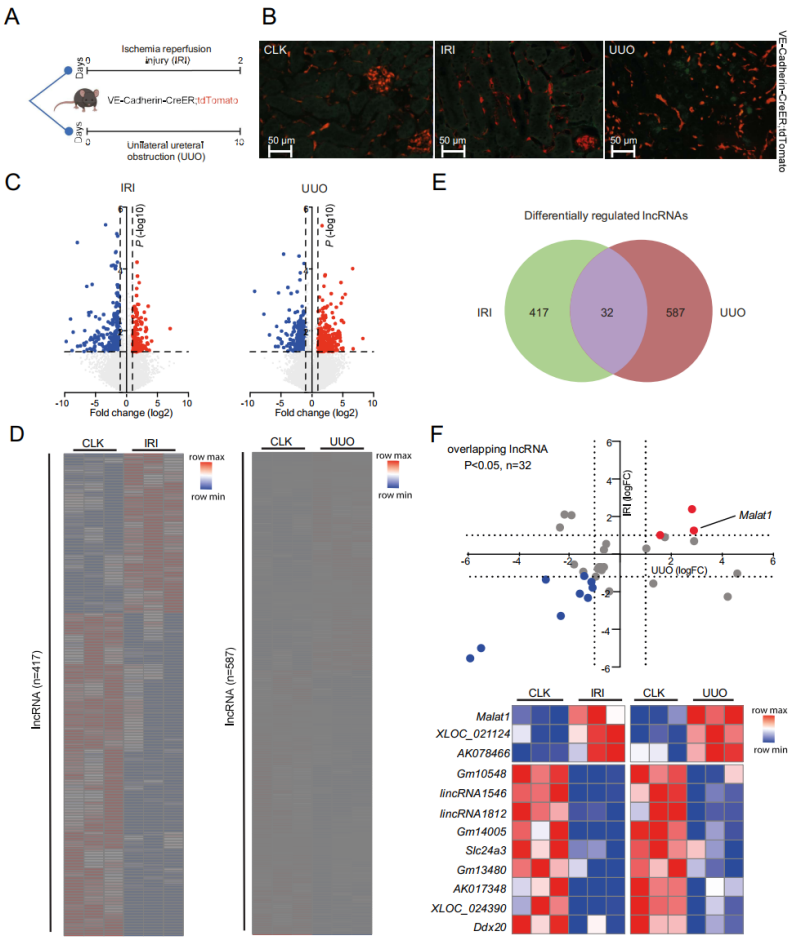

Figure 1. Loss of vascular integrity during kidney fibrosis and differential lncRNA expression in endothelial cells. (A) Schematic overview of study setup. (B) Representative images of tdTomato positive cells (red) in healthy contralateral (CLK), IRI and UUO kidneys. (C) Volcano plots visualizing differential lncRNA expression between indicated conditions. The blue and red dots correspond to lncRNAs with P<0.05 and -1<logFC>1 that are down or up regulated, respectively. Grey dots indicate non-significantly changed lncRNAs. (D) Hierarchical clustering shows a distinguishable lncRNA expression pattern in VE-cadherin derived cells in IRI and UUO compared to healthy CLK (n=3 per condition). (E) Venn diagram indicating number of differentially expressed lncRNAs in IRI and UUO. (F) Scatter plot and heatmap of lncRNAs that are significantly differentially expressed in both models. The blue and red dots correspond to lncRNAs with P<0.05 and -1<logFC>1 that are down or up regulated, respectively. Grey dots indicate non-significantly changed lncRNAs.

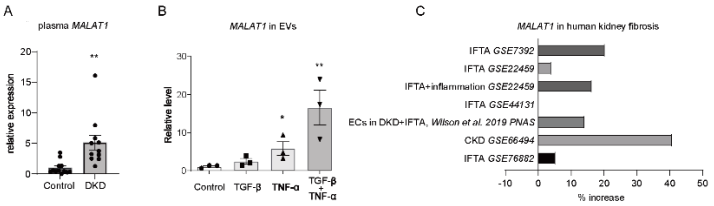

Figure 2. Increased kidney and circulating *MALAT1* levels in fibrotic kidney disease. (A) RT-qPCR analysis of *MALAT1* levels in plasma of patients with diabetic kidney disease (DKD) and healthy controls. (B) RT-qPCR analysis of *MALAT1* in extracellular vesicles from HUVECs stimulated with TGF-β and/or TNF-α or vehicle control. (C) *MALAT1* expression levels in fibrotic kidney tissue compared to controls from different datasets. IFTA = interstitial fibrosis and tubular atrophy. CKD = chronic kidney disease. *P<0.05, **P<0.01**.**

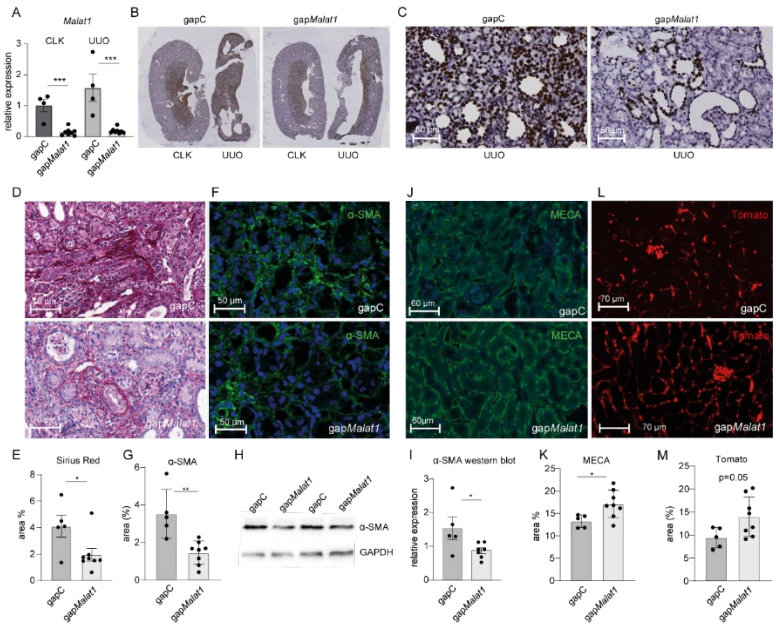

Figure 3. *In vivo Malat1* knockdown inhibits kidney fibrosis and preserves vascular integrity. (A) RT-qPCR analysis of *Malat1* in the kidney upon *Malat1* targeting GapmeR treatment (gap*Malat1*), compared to control GapmeR (gapC) treated mice. (B-C) Representative whole mount images (B) and zoomed in images (C) of *in situ* hybridization for *Malat1*. (D-E) Representative images of Sirius Red staining (D) and corresponding quantification (E). (F-G) Representative images of α-SMA staining (F) and corresponding quantification (G). (H-I) Representative western blots for α-SMA (H) and corresponding quantification (I), normalized for GAPDH. (J-K) Representative images of endothelial cell marker MECA32 (J) and corresponding quantification (K). (L-M) Representative images of endogenous Tomato label (L) and corresponding quantification (M). *P<0.05, **P<0.01, ***P<0.001. CLK = healthy contralateral kidney, UUO = fibrotic kidney from unilateral ureteral obstruction model. gapC = control GapmeR, gap*Malat1* = *Malat1* GapmeR.

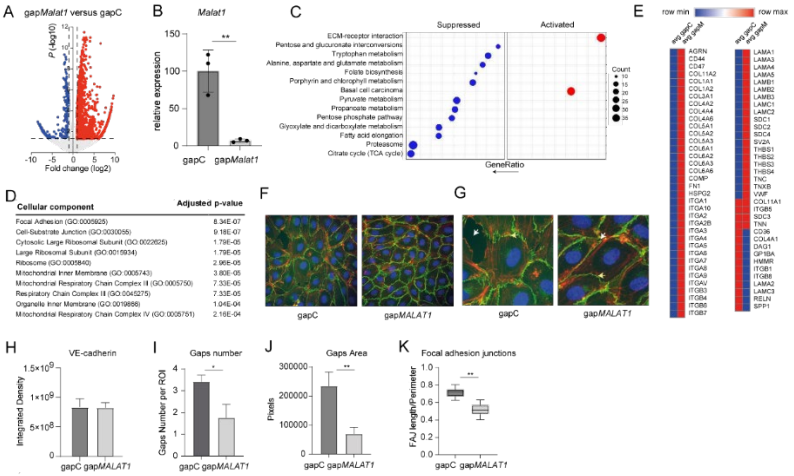

Figure 4. Knockdown of *MALAT1* affects cell-cell and cell-matrix interaction. (A) Volcano plots visualizing differential gene expression in ECs in vivo upon GapmeR-mediated *Malat1* knockdown. The blue and red dots correspond to mRNAs with P<0.05 and -1<logFC>1 that are down or up regulated, respectively. Grey dots indicate non-significantly changed mRNAs. (B) *Malat1* levels as determined by RT-qPCR on FACS-sorted mouse kidney ECs. (C-D) Gene set enrichment analyses (C) and cellular component analysis on differentially expressed genes from (A). (E) Heatmap showing relative expression of genes involved in ECM-receptor interaction. (F-G) Representative images of VE-cadherin staining (green) and F-actin (red) (zoomed images in (G)) on HUVECs treated with gap*MALAT1* or gapC, in the presence of TGF-β. Example of gaps (loss cell-cell contacts) are shown by white arrows and focal adhesion junctions by yellow arrows. (H-K) Quantification of total VE-cadherin staining (H), number of gaps (loss of cell-cell contacts) (I), area of gaps (J) and focal adhesion junctions (K). *P<0.05, **P<0.01.

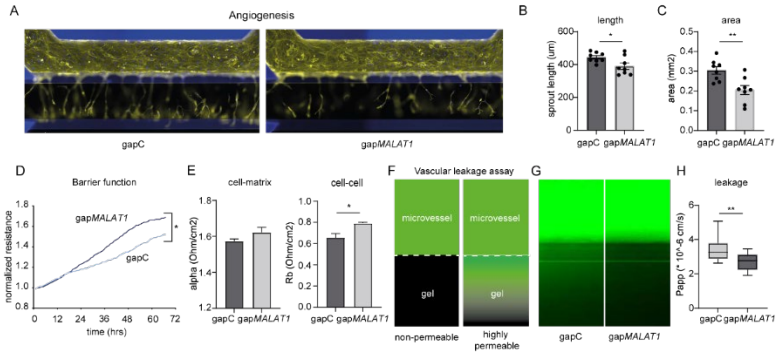

Figure 5. Knockdown of *MALAT1* in ECs increases barrier function and reduces angiogenesis. (A-C) Representative images (A) of VEGF, bFGF and S1P induced angiogenesis upon knockdown of *MALAT1* (gap*MALAT1*) or control (gapC) and corresponding quantification of average sprout length (B) and total area (C). (D-E) Trans-endothelial electrical resistance of ECs after treatment with gap*MALAT1* or gapC over time (D), attributable to cell-matrix contacts (alpha) and cell-cell contacts (Rb) (E). (F) Schematic representation of the leakage assay, with HUVEC-based 3D capillary-like vessels in the upper perfusion channel, separated from a collagen gel in the lower channel with a phaseguide. Leak tight vessels have limited leakage of fluorescently labeled albumin, while increased permeability of the vessels results in increased fluorescent signal in the gel channel. (G-H) Analysis of leakage assay after knockdown of *MALAT1* (gap*MALAT1*) or control (gapC) in HUVECs presented in (F). Representative photographs (G) and quantification of the permeability of capillary-like vessels (H). *P<0.05, **P<0.01.

References

1. Collaboration, G.B.D.C.K.D. Global, regional, and national burden of chronic kidney disease, 1990-2017: a systematic analysis for the Global Burden of Disease Study 2017. *Lancet* **395**, 709-733 (2020).
2. Levey, A.S. & Coresh, J. Chronic kidney disease. *Lancet* **379**, 165-180 (2012).
3. Kalantar-Zadeh, K., Jafar, T.H., Nitsch, D., Neuen, B.L. & Perkovic, V. Chronic kidney disease. *Lancet* **398**, 786-802 (2021).
4. Long, D.A., Norman, J.T. & Fine, L.G. Restoring the renal microvasculature to treat chronic kidney disease. *Nat Rev Nephrol* **8**, 244-250 (2012).
5. Choi, Y.J., Chakraborty, S., Nguyen, V.*, et al.* Peritubular capillary loss is associated with chronic tubulointerstitial injury in human kidney: altered expression of vascular endothelial growth factor. *Hum Pathol* **31**, 1491-1497 (2000).
6. Seron, D., Alexopoulos, E., Raftery, M.J., Hartley, B. & Cameron, J.S. Number of interstitial capillary cross-sections assessed by monoclonal antibodies: relation to interstitial damage. *Nephrol Dial Transplant* **5**, 889-893 (1990).
7. Rabelink, T.J., Wijewickrama, D.C. & de Koning, E.J. Peritubular endothelium: the Achilles heel of the kidney? *Kidney Int* **72**, 926-930 (2007).
8. Ishii, Y., Sawada, T., Kubota, K.*, et al.* Injury and progressive loss of peritubular capillaries in the development of chronic allograft nephropathy. *Kidney Int* **67**, 321-332 (2005).
9. Lorenzen, J.M. & Thum, T. Long noncoding RNAs in kidney and cardiovascular diseases. *Nat Rev Nephrol* **12**, 360-373 (2016).
10. Bink, D.I., Pauli, J., Maegdefessel, L. & Boon, R.A. Endothelial microRNAs and long noncoding RNAs in cardiovascular ageing. *Atherosclerosis* **374**, 99-106 (2023).
11. Mattick, J.S., Amaral, P.P., Carninci, P.*, et al.* Long non-coding RNAs: definitions, functions, challenges and recommendations. *Nat Rev Mol Cell Biol* **24**, 430-447 (2023).
12. Wang, P., Luo, M.L., Song, E.*, et al.* Long noncoding RNA lnc-TSI inhibits renal fibrogenesis by negatively regulating the TGF-beta/Smad3 pathway. *Sci Transl Med* **10**(2018).
13. Bijkerk, R., Au, Y.W., Stam, W.*, et al.* Long Non-coding RNAs Rian and Miat Mediate Myofibroblast Formation in Kidney Fibrosis. *Front Pharmacol* **10**, 215 (2019).
14. Stanicek, L., Lozano-Vidal, N., Bink, D.I.*, et al.* Long non-coding RNA LASSIE regulates shear stress sensing and endothelial barrier function. *Commun Biol* **3**, 265 (2020).
15. Wang, Y., Nakayama, M., Pitulescu, M.E.*, et al.* Ephrin-B2 controls VEGF-induced angiogenesis and lymphangiogenesis. *Nature* **465**, 483-486 (2010).
16. Groeneweg, K.E., Au, Y.W., Duijs, J.*, et al.* Diabetic nephropathy alters circulating long noncoding RNA levels that normalize following simultaneous pancreas-kidney transplantation. *Am J Transplant* **20**, 3451-3461 (2020).
17. Hopper, R.K., Moonen, J.R., Diebold, I.*, et al.* In Pulmonary Arterial Hypertension, Reduced BMPR2 Promotes Endothelial-to-Mesenchymal Transition via HMGA1 and Its Target Slug. *Circulation* **133**, 1783-1794 (2016).
18. Qi, C., Bin, L., Yang, Y.*, et al.* Glipizide suppresses prostate cancer progression in the TRAMP model by inhibiting angiogenesis. *Sci Rep* **6**, 27819 (2016).
19. Camos, S., Gubern, C., Sobrado, M.*, et al.* The high-mobility group I-Y transcription factor is involved in cerebral ischemia and modulates the expression of angiogenic proteins. *Neuroscience* **269**, 112-130 (2014).
20. Wilson, P.C., Wu, H., Kirita, Y.*, et al.* The single-cell transcriptomic landscape of early human diabetic nephropathy. *Proc Natl Acad Sci U S A* **116**, 19619-19625 (2019).

21. Huveneers, S., Oldenburg, J., Spanjaard, E.*, et al.* Vinculin associates with endothelial VE-cadherin junctions to control force-dependent remodeling. *J Cell Biol* **196**, 641-652 (2012).
22. Zhang, B., Arun, G., Mao, Y.S.*, et al.* The lncRNA Malat1 is dispensable for mouse development but its transcription plays a cis-regulatory role in the adult. *Cell Rep* **2**, 111-123 (2012).
23. Wang, Y., Song, F., Zhang, B.*, et al.* The 3D Genome Browser: a web-based browser for visualizing 3D genome organization and long-range chromatin interactions. *Genome Biol* **19**, 151 (2018).
24. Clarke, D.J.B., Marino, G.B., Deng, E.Z.*, et al.* Rummagene: massive mining of gene sets from supporting materials of biomedical research publications. *Commun Biol* **7**, 482 (2024).
25. D, G.H., Kelley, D.R., Tenen, D., Bernstein, B. & Rinn, J.L. Widespread RNA binding by chromatin-associated proteins. *Genome Biol* **17**, 28 (2016).
26. Fan, Y., Shen, B., Tan, M.*, et al.* TGF-beta-induced upregulation of malat1 promotes bladder cancer metastasis by associating with suz12. *Clin Cancer Res* **20**, 1531-1541 (2014).
27. West, J.A., Davis, C.P., Sunwoo, H.*, et al.* The long noncoding RNAs NEAT1 and MALAT1 bind active chromatin sites. *Mol Cell* **55**, 791-802 (2014).
28. Bijkerk, R., de Bruin, R.G., van Solingen, C.*, et al.* MicroRNA-155 functions as a negative regulator of RhoA signaling in TGF-beta-induced endothelial to mesenchymal transition. *Microrna* **1**, 2-10 (2012).
29. van Duinen, V., van den Heuvel, A., Trietsch, S.J.*, et al.* 96 perfusable blood vessels to study vascular permeability in vitro. *Sci Rep* **7**, 18071 (2017).
30. Goligorsky, M.S. Permissive role of vascular endothelium in fibrosis: focus on the kidney. *Am J Physiol Cell Physiol* **326**, C712-C723 (2024).
31. Michalik, K.M., You, X., Manavski, Y.*, et al.* Long noncoding RNA MALAT1 regulates endothelial cell function and vessel growth. *Circ Res* **114**, 1389-1397 (2014).
32. Wang, C., Qu, Y., Suo, R. & Zhu, Y. Long non-coding RNA MALAT1 regulates angiogenesis following oxygen-glucose deprivation/reoxygenation. *J Cell Mol Med* **23**, 2970-2983 (2019).
33. Liu, J.Y., Yao, J., Li, X.M.*, et al.* Pathogenic role of lncRNA-MALAT1 in endothelial cell dysfunction in diabetes mellitus. *Cell Death Dis* **5**, e1506 (2014).
34. Liu, S.X., Zheng, F., Xie, K.L.*, et al.* Exercise Reduces Insulin Resistance in Type 2 Diabetes Mellitus via Mediating the lncRNA MALAT1/MicroRNA-382-3p/Resistin Axis. *Mol Ther Nucleic Acids* **18**, 34-44 (2019).
35. Yao, R.W., Wang, Y. & Chen, L.L. Cellular functions of long noncoding RNAs. *Nat Cell Biol* **21**, 542-551 (2019).
36. Lino Cardenas, C.L., Kessinger, C.W., Cheng, Y.*, et al.* An HDAC9-MALAT1-BRG1 complex mediates smooth muscle dysfunction in thoracic aortic aneurysm. *Nat Commun* **9**, 1009 (2018).
37. Yin, Y., Lu, J.Y., Zhang, X.*, et al.* U1 snRNP regulates chromatin retention of noncoding RNAs. *Nature* **580**, 147-150 (2020).
38. Morini, M.F., Giampietro, C., Corada, M.*, et al.* VE-Cadherin-Mediated Epigenetic Regulation of Endothelial Gene Expression. *Circ Res* **122**, 231-245 (2018).
39. Liu, P., Zhang, B., Chen, Z.*, et al.* m(6)A-induced lncRNA MALAT1 aggravates renal fibrogenesis in obstructive nephropathy through the miR-145/FAK pathway. *Aging (Albany NY)* **12**, 5280-5299 (2020).
40. Xia, W., Chen, X., Zhu, Z.*, et al.* Knockdown of lncRNA MALAT1 attenuates renal interstitial fibrosis through miR-124-3p/ITGB1 axis. *Sci Rep* **13**, 18076 (2023).
41. Tripathi, V., Ellis, J.D., Shen, Z.*, et al.* The nuclear-retained noncoding RNA MALAT1 regulates alternative splicing by modulating SR splicing factor phosphorylation. *Mol Cell* **39**, 925-938 (2010).

42. Cui, H., Banerjee, S., Guo, S*., et al.* Long noncoding RNA Malat1 regulates differential activation of macrophages and response to lung injury. *JCI Insight* **4**(2019).
43. Hu, M., Wang, R., Li, X*., et al.* LncRNA MALAT1 is dysregulated in diabetic nephropathy and involved in high glucose-induced podocyte injury via its interplay with beta-catenin. *J Cell Mol Med* **21**, 2732-2747 (2017).
44. Kolling, M., Genschel, C., Kaucsar, T*., et al.* Hypoxia-induced long non-coding RNA Malat1 is dispensable for renal ischemia/reperfusion-injury. *Sci Rep* **8**, 3438 (2018).
45. Fawzy, M.S., Abu AlSel, B.T., Al Ageeli, E*., et al.* Long non-coding RNA MALAT1 and microRNA-499a expression profiles in diabetic ESRD patients undergoing dialysis: a preliminary cross-sectional analysis. *Arch Physiol Biochem* **126**, 172-182 (2020).
46. Uil, M., Hau, C.M., Ahdi, M*., et al.* Cellular origin and microRNA profiles of circulating extracellular vesicles in different stages of diabetic nephropathy. *Clin Kidney J* **14**, 358-365 (2021).
47. Rodrigues, K.F., Pietrani, N.T., Fernandes, A.P*., et al.* Circulating microparticles levels are increased in patients with diabetic kidney disease: A case-control research. *Clin Chim Acta* **479**, 48-55 (2018).
48. Burger, D., Turner, M., Xiao, F*., et al.* High glucose increases the formation and pro-oxidative activity of endothelial microparticles. *Diabetologia* **60**, 1791-1800 (2017).
49. Vreeken, D., et al. Downregulation of Endothelial Plexin A4 Under Inflammatory Conditions Impairs Vascular Integrity. *Front Cardiovasc Med* **8**, 633609 (2021).
50. van Duinen, V., et al. Standardized and Scalable Assay to Study Perfused 3D Angiogenic Sprouting of iPSC-derived Endothelial Cells In Vitro. *J Vis Exp* (2019).

Supplementary Figures

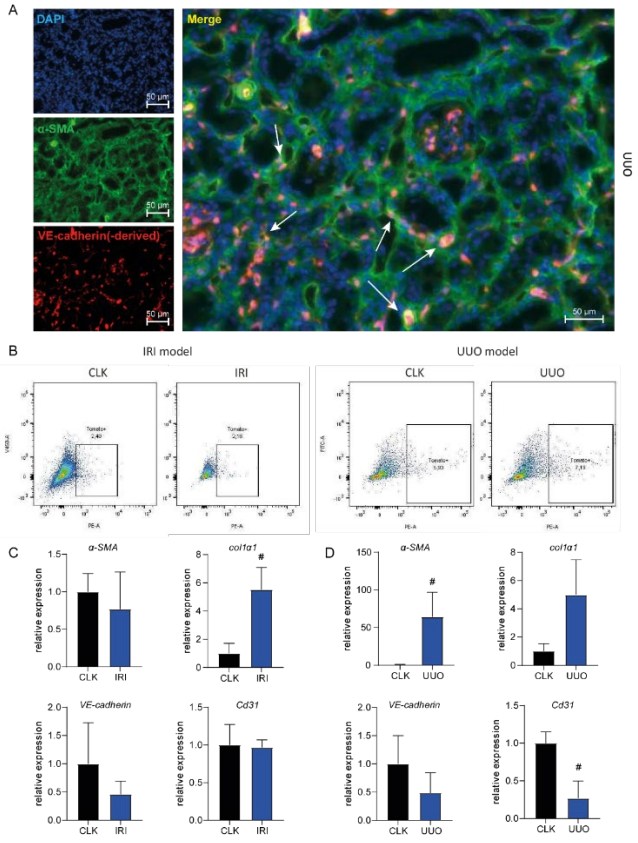

Supplementary Figure 1. Endothelial-to-mesenchymal transition in murine kidney fibrosis. (A) representine image of co-localization (examples are indicated with arrows) of VE-cadherin-derived tomato positive cells and α-SMA stained positive cells in a UUO kidney. (B) Representative FACS plots for isolation of Tomato-positive VE-Cadherin-derived cells. (C-D) qPCR was performed for endothelial cell genes (Cd31 and Cdh5 (VE-cadherin)) and mesenchymal/myofibroblast genes (Acta2 (α-SMA) and Col1α1) on FACS sorted cells from VE-cadherin-tomato mice in the IRI model (C) and UUO model (D). $^{\#}P<0.10$.

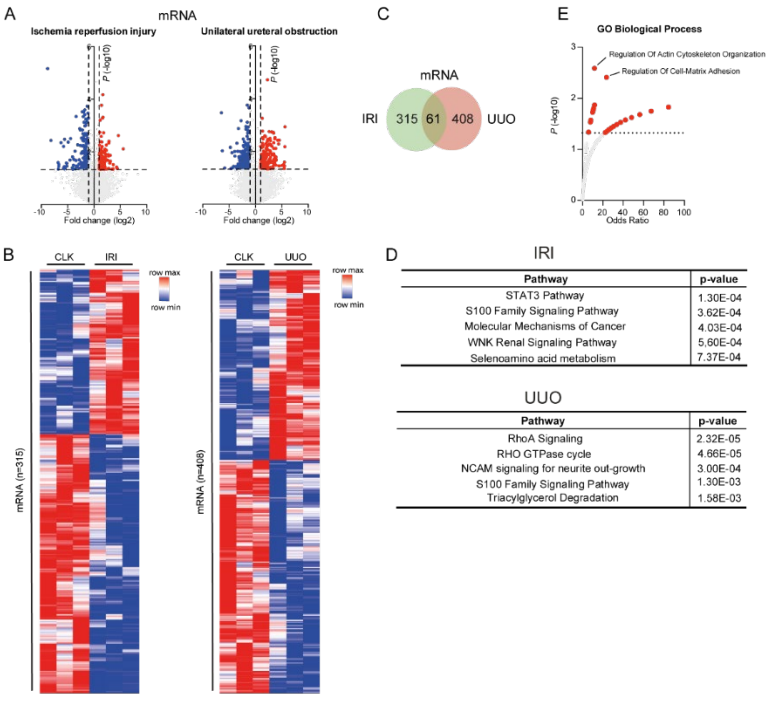

Supplementary Figure 2. Differential mRNA expression in endothial (-derived) cells in IRI and UUO. (A) Volcano Plots are visualizing differential mRNA expression between indicated conditions. The blue and red dots correspond to mRNAs with P<0.05 and -1<logFC>1 that are down or up regulated, respectively. (B) Hierarchical clustering shows a distinguishable mRNA expression pattern in VE-cadherin derived cells in IRI and UUO compared to healthy contralateral kidneys (CLK) (n=3 per condition). (C) VENN diagram showing total number of differentially expressed genes per model as well as overlapping genes. (D) Ingenuity Pathway analyses indicates predicted enriched pathways. (E) GO analysis of biological pathways among the 61 overlapping genes between IRI and UUO are involved in actin cytoskeleton regulation and cell-matrix iadhesion.

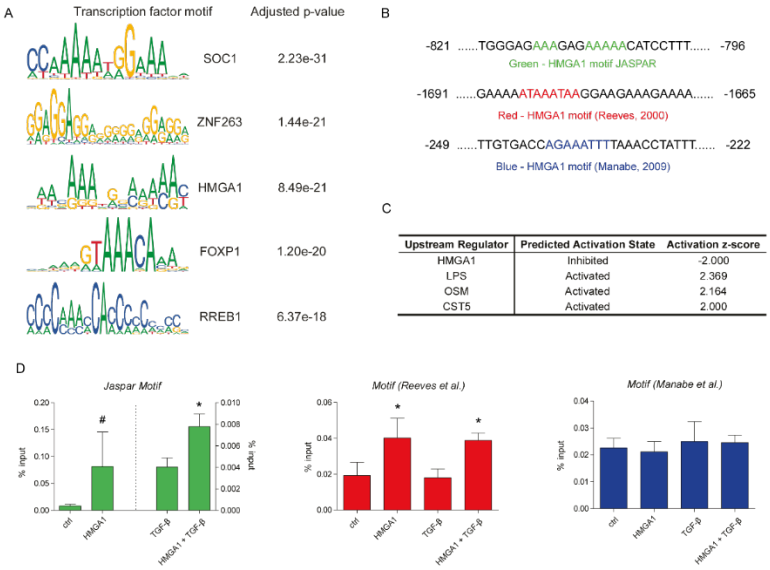

Supplementary Figure 3. (A) Transcription factor motif enrichment analysis (JASPAR Core 2016) indicates enriched transcription factor motifs in promoter regions of differentially expressed lncRNAs. Top 5 (p-value) is depicted. (B) Within the promoter region of Malat1 (defined as <2000 bp upstream of the start site) we found 3 potential HMGA1 binding motifs. In addition to the identified JASPAR motif for HMGA1, two additional potential binding motifs for HMGA1 were identfied from literature (Reeves, 2000, Environ Health Perspect & Manabe et al., 2009, PLoS One). (C) Pathway analysis on differential mRNA profiles (Supplementary Figure 2) predicts HMGA1 to be a negatively regulated upstream regulator of differentially expressed genes in ECs in UUO. (D) PCR for Malat1 promoter regions following HMGA1 ChIP, with IgG as negative control. *P<0.05, #P<0.10

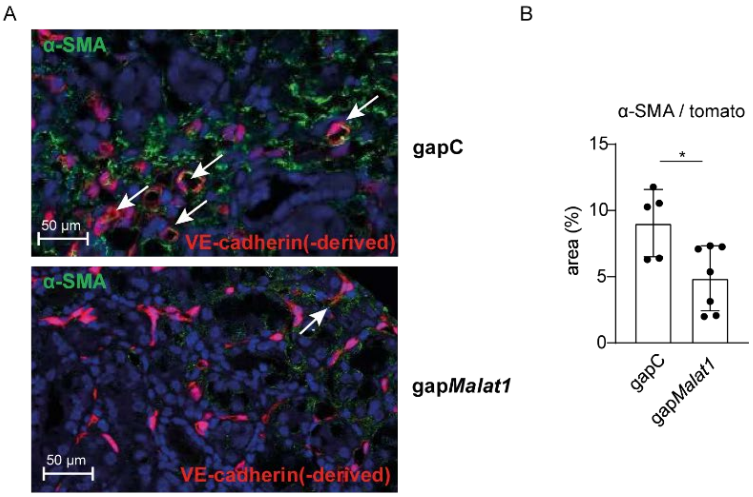

Supplementary Figure 4. In vivo Malat1 knockdown reduces endothelial to mesenchymal transition. (A-B) representine images (A) and quantification (B) of co-localization (examples are indicated with arrows) of VE-cadherin-derived tomato positive cells and α-SMA stained positive cells in a UUO kidneys from mice treated with control gapmer (gapC) or gapmer against Malat1 (gapMalat1).

Ingenuity Canonical Pathways	Z-score
Oxidative Phosphorylation	-6.564
Neutrophil Extracellular Trap Signaling Pathway	-4.621
Mitochondrial Dysfunction	4.608
Phagosome Formation	4.536
CREB Signaling in Neurons	4.158
Granzyme A Signaling	4.123
EIF2 Signaling	-3.962
Pathogen Induced Cytokine Storm Signaling Pathway	3.772
S100 Family Signaling Pathway	3.592
FAK Signaling	3.528

Supplementary Figure 5. Ingenuity Pathway analysis. Top 10 enriched canonical pathways as determined by ingenuity pathway analysis in differentially expressed genes in mouse kidney FACS-sorted ECs from mice treated with Malat1-targeting gapmer**.**

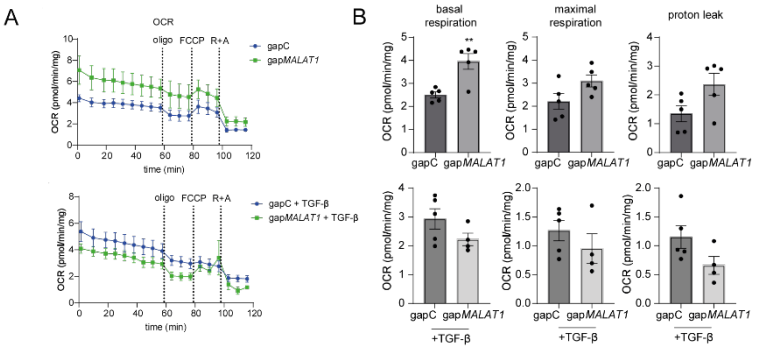

Supplementary Figure 6. Effect of MALAT1 knockdown on mitochondrial function. (A-B) Oxygen consumption rate, as determined by the Seahorse assay in HUVECs treated with gapmer against MALAT1 (gapMALAT1) or gapmer control (gapC) with (lower panel) or without treatment with TGF-β (upper panel) (A) and corresponding quantification of basal respiration, maximal respiration and proton leak (B). **P<0.01

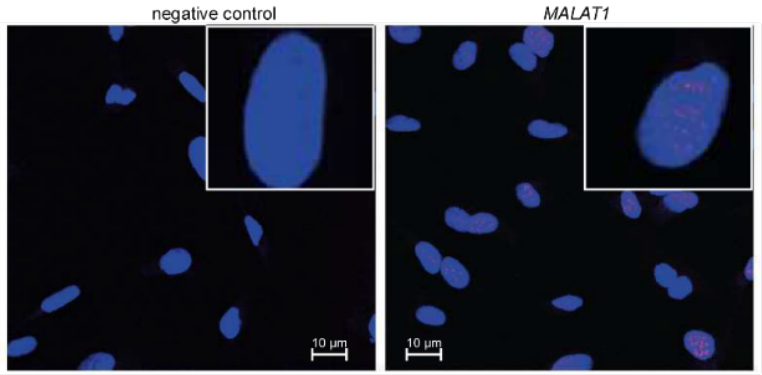

Supplementary Figure 7. FISH HUVEC. Fluorescent in situ hybridization on HUVECs for MALAT1 indicates nuclear localization. Upper right panel is zoomed in image of one nucleus.

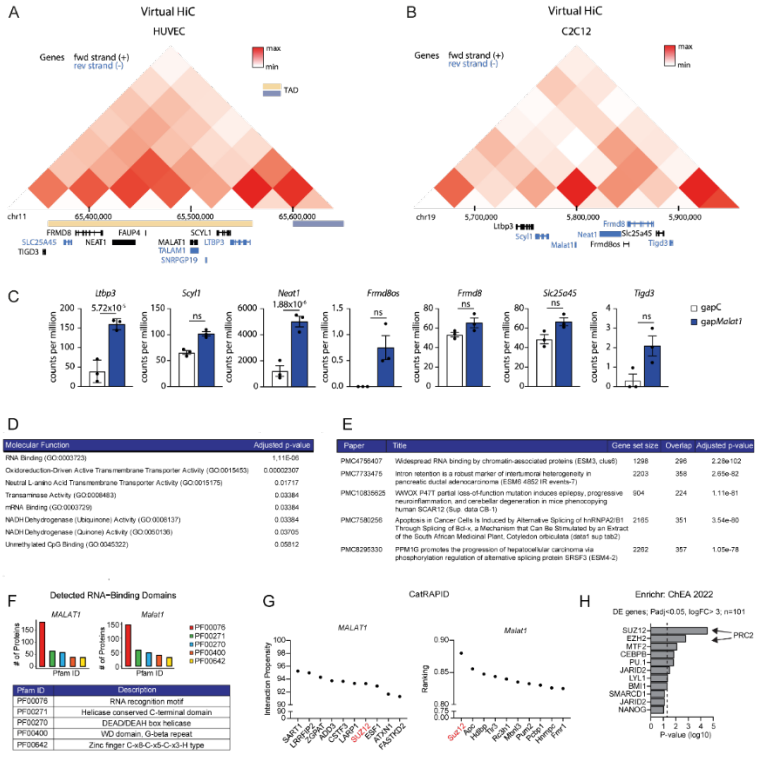

Supplementary Figure 8. Virtual HiC analysis indicates possible coregulation with Neat1, while MALAT1 potentially functions via binding SUZ12. (A) Virtual HiC analysis was performed on HUVECs to identify potential MALAT1-coregulatory genes in endothelial cells. (B) C2C12 cells were used to allow identification of mouse Malat1-neighbouring and coregulatory genes. (C) Expression of Malat1 neighbouring genes in our RNA-seq data from sorted mouse kidney endothelial cells after gapMalat1 treatment or gapC control. (D) Gene set enrichment analysis predicts enriched molecular functions based on differentially expressed genes in sorted endothelial cells from mouse kidneys upon Malat1 knockdown. (E) 'Rummagene' analysis compared DE genes with other datasets and found largely overlapping datasets. In parentheses the specific subset of data is indicated that overlaps. (F) RNA-binding domain prediction analysis of both human and mouse MALAT1. (G) CatRAPID analysis of both human and mouse MALAT1 estimates the binding propensity of proteins and a.o. finds SUZ12 is highly likely to bind MALAT1. (H) ChEA analysis on DE genes in our dataset indicates SUZ12 indeed is enriched.

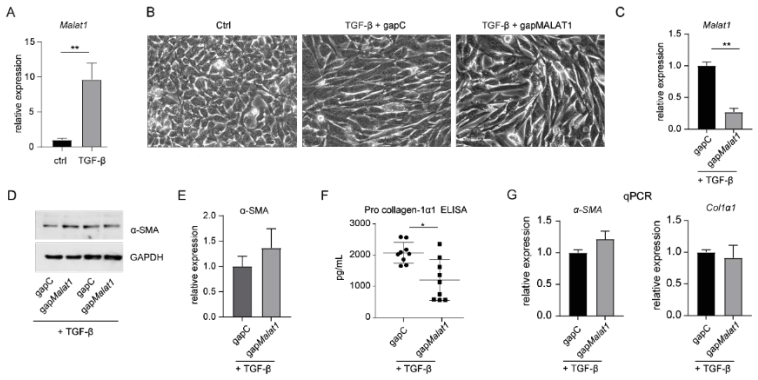

Supplementary Figure 9. Malat1 knockdown during endothelial to mesenchymal transition does not alter α-SMA but decreases collagen deposition. (A) Malat1 expression increases in TGF-β stimulated mouse ECs. (B) Representative microscopic images of mouse ECs that undergo endothelial to mesenchymal transition upon TGF-β treatment, visible from the elongated morphology. (C) Malat1 was inhibited using GapmeRs and compared to GapmeR control. (D-E) Representative western blots indicate TGF-β induces α-SMA protein expression, while this is not affected by Malat1 inhibition. (F) Malat1 knockdown decreased pro collagen1α1 levels as determined by ELISA. (G) Gene expression levels of myofibroblast marker α-SMA and fibrotic marker collagen1α1 did not change upon Malat1 gapmer. *P<0.05, **P<0.01.